JOURNAL OF AIRCRAFT
Vol. 43, No. 2, March–April 2006

Solution for Aircraft Anti-Icing System Simulation by a Modified Perturbation Method

Sumio Kato*
Kawasaki Heavy Industries, Ltd., Kakamigahara City 504-8710, Japan

A solution of the surface temperature and the runback water mass flow rate distributions along the body contour for an electrothermal or a hot-air anti-icing system of an aircraft, when water droplets impinge on the surface, is obtained by a modified perturbation method. In the method, a small dimensionless parameter α that represents the ratio of the external convective heat transfer rate from the airfoil surface to the internal heating rate is used. Because of the high nonlinearity in the energy equation, obtaining a convergent solution by normal use of the perturbation method is virtually impossible. To improve the convergence properties of the solution, the calculation procedure is modified. The main idea behind the modification is splitting of the nonlinear term into linear and nonlinear terms and introducing a new variable ε, by which α in each linear term is replaced. These modifications of the perturbation method help reduce the contribution of the nonlinear term, which drastically improves the convergence characteristics of the solution. The solutions agree well with the results obtained by the Runge–Kutta method and experimental and numerical results found in literature.

Nomenclature

a, b	=	constant parameters used to approximate $P_{v,w}$, Pa/K and Pa, respectively
C_a	=	specific heat of air, 1004 J/kg · K
C_w	=	specific heat of water, 4182 J/kg · K
c	=	chord length or characteristic length, m
F	=	wetness factor (fraction of the surface that is wetted by the runback water)
f^*, g^*	=	$r_c u_e^2/(2C_a\Delta T_1)$ and $u_\infty^2/(2C_w\Delta T_1)$
h	=	heat transfer coefficient, W/(m^2 · K)
h_{ha}	=	internal heat transfer coefficient between the hot airflow and the inner surface of the wing or the cowl, W/(m^2 · K)
h_{har}	=	$h_{\mathrm{ha}}/h_{\mathrm{ha},m}$
h_s	=	heat transfer coefficient between the outer flow and the outer surface of the wing or the cowl, W/(m^2 · K)
h_{sr}	=	$h_s/h_{s,m}$
L_a, L_b	=	3133.84 × 10^3 J/kg and 2.351 × 10^3 J/(kg · K)
L_v	=	latent heat of evaporation of water, $L_a - L_b T_w$, J/kg
L_a^*, L_b^*, L_v^*	=	$L_a/(C_a\Delta T_1)$, L_b/C_a, and $L_v/(C_a\Delta T_1)$
M	=	molecular mass, kg/kmol
$\dot{m}'$	=	runback water mass flow rate per unit width, kg/m · s
$\dot{m}'^*$	=	$\dot{m}' C_w\Delta T_1/(q_{\mathrm{ht},m}c)$ or $\dot{m}' C_w\Delta T_1/(h_{\mathrm{ha},m}\Delta T_2 c)$
$\dot{m}'_{\mathrm{in}}$, $\dot{m}'_{\mathrm{out}}$	=	$\dot{m}'$ flowing into and out of the control volume, respectively
$\dot{m}''$	=	water mass flux, kg/m^2 · s
$\dot{m}''_{\mathrm{evap}}$	=	water mass flux of evaporation per unit area of runback water, kg/m^2 · s
$\dot{m}''^*_{\mathrm{evap}}$	=	$\dot{m}''_{\mathrm{evap}} C_w\Delta T_1/q_{\mathrm{ht},m}$ or $\dot{m}''_{\mathrm{evap}} C_w\Delta T_1/(h_{\mathrm{ha},m}\Delta T_2)$
$\dot{m}''_{\mathrm{imp}}$	=	water mass flux of impingement, kg/m^2 · s
$\dot{m}''_{\mathrm{imp}}$	=	$\dot{m}''_{\mathrm{imp}} C_w\Delta T_1/q_{\mathrm{ht},m}$ or $\dot{m}''_{\mathrm{imp}} C_w\Delta T_1/(h_{\mathrm{ha},m}\Delta T_2)$
P	=	pressure, Pa
P_e	=	pressure at the edge of the boundary layer, Pa
Pr	=	Prandtl number
$P_{v,w}$	=	saturation vapor pressure of water at the outer surface of the wing or the cowl, Pa
$P_{v,\infty}$	=	saturation vapor pressure in freestream, Pa
q	=	energy rate per unit length, W/(m · s)
q_{ha}	=	heat flux from the hot air to the inner surface of the wing or the cowl, $h_{\mathrm{ha}}(T_{\mathrm{hotair}} - T_w)$, W/m^2
q_{har}	=	$q_{\mathrm{ha}}/(h_{\mathrm{ha},m}\Delta T_2) = h_{\mathrm{har}}(\Delta T_1/\Delta T_2)(T^*_{\mathrm{hotair}} - T^*_w)$
q_{ht}	=	heat flux from electric heaters to the inner surface of the wing or the cowl, W/m^2
q_{htr}	=	$q_{\mathrm{ht}}/q_{\mathrm{ht},m}$
q_{sk}	=	q_{ht} or q_{ha}, W/m^2
r_c	=	recovery factor
Sc	=	Schmidt number
T, T^*	=	temperature, K or °C and $T/\Delta T_1$
T_{hotair}	=	temperature of the hot air
T_{ref}	=	reference temperature, 273.15 K
u	=	velocity, m/s
x, Δx	=	surface distance from the stagnation point and increment of x, m
x^*	=	x/c
α	=	$h_{s,m}\Delta T_1/q_{\mathrm{ht},m}$ or $h_{s,m}\Delta T_1/(h_{\mathrm{ha},m}\Delta T_2)$
β_{col}	=	collection efficiency
ΔT_1	=	reference temperature difference, 1 K or 1°C
ΔT_2	=	$T_{\mathrm{hotair},m} - T_{\mathrm{ref}}$
ε	=	parameter with the same value as α
ν_a, ν_w	=	kinematic viscosity of air and water, respectively
Φ	=	relative humidity
φ_{evap}	=	$(Pr/Sc)^{2/3} M_{\mathrm{water}}/M_{\mathrm{air}}$

Subscripts

a or air	=	air
e	=	evaluated at the edge of boundary layer
evap	=	evaporating from the surface
ha or hotair	=	hot air
ht	=	heater
imp	=	impingement on the surface
,m	=	maximum value or characteristic value
s	=	outer surface of the wing or the cowl
vap or v	=	vapor
v, w	=	saturated vapor of water
w or water	=	water
∞	=	freestream condition

Superscript

$*$	=	dimensionless value

Received 23 September 2004; revision received 6 January 2005; accepted for publication 9 January 2005.

*Chief, Aerospace Systems Department, Engineering Division, Aerospace Company, 1.Kawasaki-cho, Gifu-Prefecture.

Introduction

WHEN an aircraft flies through a cloud that contains supercooled water droplets at or below the freezing ambient temperature, the water droplets may impinge on the critical surfaces of the aircraft and ice accretion results when they freeze. Ice formation generally occurs on the leading-edge surfaces of wings and engine nacelles and, therefore, detrimentally affects the aircraft performance, with a serious threat to the flight safety. To predict and evaluate the performance of an aircraft in icing conditions, various ice accretion codes[1−3] have been developed and used.

Two kinds of in-flight ice protection systems can be used to prevent ice accretion on critical surfaces of an aircraft[4]: a de-icing system and an anti-icing system. The de-icing system works periodically and removes the accreted ice by mechanical or thermal means. The anti-icing system works continuously from the start of any ice accretion event, aiming for no accretion on the critical surfaces during flight at any time.

Anti-icing systems, to prevent ice accretion, usually use heat that comes either from electrical heaters installed in a metal skin or the hot bleed air flowing along the inner side of a metal skin. Some studies have been carried out concerning thermal anti-icing system simulations.[5−15] In Refs. 5 and 6, studies of a running wet anti-icing system are carried out, where the enthalpy change due to the flow of runback water from the direct impingement region to the downstream region is neglected. Heinrich et al.[7] investigated a simplified procedure for predicting and evaluating engine inlet anti-icing systems of the hot-air type, in which the temperature distribution of the runback water along the contour of the body in the airflow direction is calculated and compared with the experimental results. Al-Khalil et al.[8] and Al-Khalil[9] analyzed an anti-icing system for an engine inlet with a one-dimensional heat transfer model for the runback water. This model treats the runback water and the solid wall as two separate regions and the temperature gradient across the thickness within each region is assumed to be negligible, whereas the enthalpy transport in the liquid region is taken into account. This model is referred to as the basic anti-icing model. Al-Khalil[9] and Al-Khalil, et al.[10,11] also developed a two-dimensional heat transfer model for the runback water and the solid wall. The water runs down as a continuous film flow in the impingement region. The continuous film flow breaks up outside of the impingement region into individual rivulets when a minimum critical thickness is reached. The wetness factor distribution resulting from the breakup and the rivulet configuration on the surface are predicted using a stability analysis theory and laws of mass and energy conservation. The temperature distribution in the runback water and the wall in the two-dimensional model is calculated by a numerical method. This model is referred to as the improved anti-icing model. Morency et al.[12,13] analyzed an anti-icing system by using a two-dimensional runback model. The temperature gradient across the thin layer of the runback water and the surface temperature distribution in the flow direction along a streamline on the surface are solved by an iterative procedure. These works concerning the anti-icing system simulation mentioned earlier calculated the surface temperature and the runback water mass flow rate distributions of an anti-icing system by numerical methods such as the finite difference methods.

Generally, the mathematical and computational procedure involved in the simulation of an aircraft anti-icing system contains the following steps:

1) The critical aerodynamic surface is modeled and represented by many discrete grid points or panels.

2) The airflow is calculated on and about the surface by a flowfield solver.

3) The liquid water droplet trajectories are computed to determine the rate of water impingement on the surface.

4) With the results of steps 2 and 3 as inputs, a thermal or thermodynamic analysis is performed on the runback water on the surface and the solid wall.

For the design of an aircraft anti-icing system, a lot of calculations are necessary in step 4 to study the effect of parameters, such as ambient conditions, heating rates from inner side of the wall, and minimum heating requirements, on the performance of the anti-icing system. These parametric studies in step 4 can be conducted by using numerical methods. However, if a simple analytical solution is available in step 4, it would be easier to handle with the analytical solution rather than a numerical solution. Moreover, the simplicity of the analytical solution will help better understand the relation between these parameters and the performance of the anti-icing system, and parametric studies for the anti-icing system will be more easily carried out compared with using a numerical solution.

With regard to the heat transfer model in which the enthalpy change due to the runback water flow is taken into account, to the author's knowledge no analytical solutions for a thermal anti-icing system have been investigated in literature.

In this paper, a solution of the surface temperature and the runback water mass flow rate distributions along the body contour for an electrothermal or a hot-air anti-icing system of an aircraft, when water droplets impinge on the surface, is obtained analytically by a modified perturbation method. Whereas the improved anti-icing model[9−11] and the model of Morency et al.[12,13] are based on two-dimensional heat transfer formulations, the heat transfer model in the present study is based on a one-dimensional heat transfer formulation. The temperature gradient across the combined metal skin and water film thickness is assumed to be negligible. The enthalpy transport in the runback water is taken into account, and the temperature varies in the flow direction along the streamline on the surface. The wetness factor depends on the surface tension and is linked to the runback water, which the improved anti-icing model[9−11] takes into account. However in this study, the wetness factor is treated as a requirement, given as an input to the calculation, which is the same as in the case of the basic anti-icing model.[8,9] The main difference between the present model and the basic anti-icing model is that the temperatures of the runback water and the wall in the basic anti-icing model differ at the same surface location, whereas in the present model the temperatures are assumed to take the same values.

Although the range of parameters where the solution is applicable might be confined to a narrow area compared with direct numerical methods, the analytical solution in the present study has the following advantages: 1) We can study the effect of different terms and parameters on the solution and perform a parametric study with parameters such as heat source terms, heat sink terms, ambient conditions, and minimum heat requirements. The simplicity of the solution will help to understand the tendencies of the relations easily. 2) The solution is simple in that it is expressed by a power series in a small variable α and each coefficient is expressed by elementary functions of the given parameters and their integrals along the surface contour. The analytical solution needs no iteration process, which is sometimes needed for calculations by numerical methods. 3) Within the range of parameters where the solution converges, when the order of the truncated solution increases, the solution will approach an exact solution. 4) It provides a means to verify computer solutions calculated by a newly developed program. 5) It provides a simple tool for rapid calculations.

When the analytical solution is being obtained, a dimensionless small parameter α that represents the ratio of the external convective heat transfer rate from an airfoil surface to the internal heating rate is used. The latent heat energy term due to evaporation in the energy equation is nonlinear and has a large value, which makes the convergence characteristics of the solution worse. It is virtually impossible to obtain a solution by a normal use of the perturbation method. To overcome this difficulty, the following development is implemented: 1) The nonlinear latent heat term is split into linear and nonlinear terms to reduce the contribution of the nonlinearity in the equation. 2) A new variable ε is introduced, and α in each linear term of the equation is replaced by ε. 3) The solution is obtained by using the perturbation parameter α, whereas ε is considered a different variable. 4) After the solution is obtained by the perturbation method, the variable ε is considered to have the same value as α. These modifications of the perturbation method help reduce the contribution of the nonlinear term to the solution, which drastically improves the convergence characteristics of the solution.

Several examples of the analytical solution are described. The solutions presented agreed well with the numerical results obtained by

the Runge–Kutta method and also agreed well with the calculation results and the test results found in literature. The effectiveness of the solution is also discussed.

Anti-icing Analysis Model and Basic Equations

Consider a critical aerodynamic surface of an aircraft, such as that of wings and engine nacelles, impinged by supercooled water droplets in atmospheric icing conditions, where an electrothermal or a hot-air anti-icing system is activated. The mass balance and the energy balance models including control volumes on the surface are shown in Figs. 1a and 1b. On impact, the water begins to run back along the surface in the airflow direction due to the aerodynamic shear force. Assumptions for calculating the surface temperature and the runback water mass flow rate distributions are as follows:

1) The critical aerodynamic surface is made of thin metal skin. Because the runback water film thickness and the metal skin is thin, the temperature variation normal to the surface will be neglected, and both the runback water and the skin temperatures are assumed to be equal.

2) Heat conduction in the streamline direction in the runback water and the skin is negligible.

3) Variation of the temperature in the span direction is neglected.

4) The system is in steady state.

5) Only the region where the runback water remains is treated.

6) The runback water follows the streamline and the problem can, thus, become one dimensional.

7) Except for the latent heat of evaporation of water L_v and the saturation vapor pressure of water $P_{v,w}$, all physical properties in the energy equation are constant.

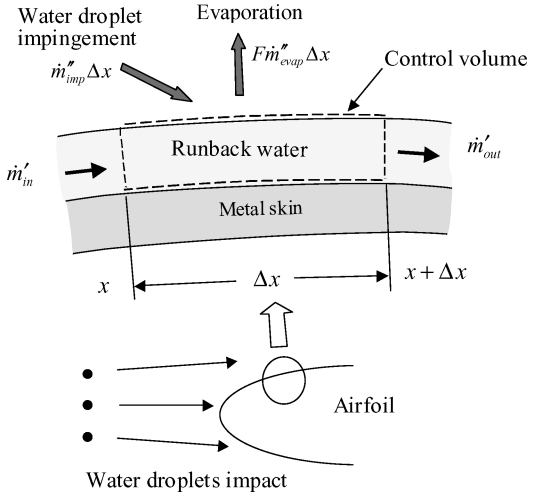

Fig. 1a Mass balance on a control volume for runback water.

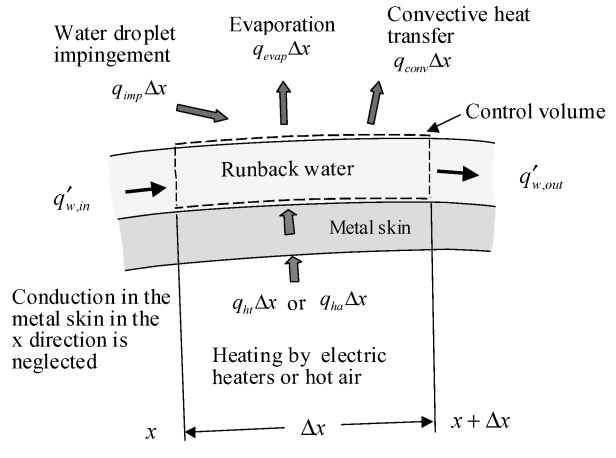

Fig. 1b Energy balance on a control volume for runback water.

A mass balance on a control volume for the runback water, as shown in Fig. 1a, yields

$$\dot{m}'_{\text{in}}(x) - \dot{m}'_{\text{out}}(x+\Delta x) + \dot{m}''_{\text{imp}}\Delta x - F\dot{m}''_{\text{evap}}\Delta x = 0 \qquad (1a)$$

Dividing Eq. (1a) by Δx and rearranging terms, we obtain[8]

$$\frac{\mathrm{d}\dot{m}'}{\mathrm{d}x} = \dot{m}''_{\text{imp}} - F\dot{m}''_{\text{evap}} \qquad (1b)$$

At the stagnation point, there is no water inflow along the surface,

$$\dot{m}' = 0 \qquad (x = 0) \qquad (2)$$

In the region of direct water impingement, the surface is fully wetted and $F = 1$. Downstream of this region, the water breaks up into individual rivulets and F decreases. Measurements during airfoil tests showed that the wetness factor rapidly decreased to approximately 0.3 at a distance of less than 0.0254 m (1 in.) downstream of the impingement limit and decreased slowly thereafter.[16] Integrating Eq. (1b) and considering Eq. (2) yields

$$\dot{m}' = \int_0^x (\dot{m}''_{\text{imp}} - F\dot{m}''_{\text{evap}})\,\mathrm{d}x \qquad (3)$$

The impingement rate of water per unit area, $\dot{m}''_{\text{imp}}$, using the liquid water content (LWC) in kilograms per cubic meter is

$$\dot{m}''_{\text{imp}} = \beta_{\text{col}}(\text{LWC})u_\infty \qquad (4)$$

Usually $\dot{m}''_{\text{imp}}$ or β_{col} takes a peak value around the stagnation point and decreases as the distance from the stagnation point increases. The evaporation rate of water per unit area is expressed by[8,9]

$$\dot{m}''_{\text{evap}} = \frac{h_s}{C_a}\left(\frac{Pr}{Sc}\right)^{\frac{2}{3}}_{\text{air}}\frac{M_{\text{water}}}{M_{\text{air}}}\left[\frac{P_{v,w} - P_{\text{vap}}}{P_e - P_{v,w}}\right] \qquad (5)$$

where P_{vap} is the local vapor pressure at the edge of the boundary layer. Application of Dalton's law of partial pressures and knowledge of ambient conditions yields[8]

$$P_{\text{vap}} = P_e(P_{v,\infty}/P_\infty)\Phi_\infty \qquad (6)$$

where Φ_∞ is taken to be 100%. The saturation vapor pressure of water at the surface, $P_{v,w}$, is[8]

$$P_{v,w} = 2337\exp[6789(1/293.15 - 1/T_w) - 5.031\,\ell_{\text{n}}(T_w/293.15)] \qquad (7)$$

An energy balance on a control volume for the runback water, as shown in Fig. 1b, gives

$$q'_{w,\text{in}}(x) - q'_{w,\text{out}}(x+\Delta x) + q_{\text{imp}}\Delta x - q_{\text{evap}}\Delta x - q_{\text{conv}}\Delta x + q_{sk}\Delta x = 0 \qquad (8a)$$

where $q'_{w,\text{in}}(x)$ is the enthalpy of the runback water flowing into the control volume, $q'_{w,\text{out}}(x+\Delta x)$ the enthalpy of the runback water flowing out of the control volume, $q_{\text{evap}}\Delta x$ the rate of energy transfer from the surface due to evaporation, $q_{\text{imp}}\Delta x$ the energy flow rate of the impinging water, $q_{\text{conv}}\Delta x$ the convective heat flow rate from the surface, and $q_{sk}\Delta x$ the heating rate from the skin. Each energy term in Eq. (8a) is expressed as follows:

$$q'_{w,\text{in}}(x) = \dot{m}'_{w,\text{in}}(x)i_w[T_w(x)]$$

$$q'_{w,\text{out}}(x+\Delta x) = \dot{m}'_{w,\text{out}}(x+\Delta x)i_w[T_w(x+\Delta x)]$$

$$q_{\text{imp}}\Delta x = \dot{m}''_{\text{imp}}\left[C_w(T_\infty - T_{\text{ref}}) + u_\infty^2/2\right]\Delta x$$

$$q_{\text{evap}}\Delta x = F\dot{m}''_{\text{evap}}[C_w(T_w - T_{\text{ref}}) + L_v]\Delta x$$

$$q_{\text{conv}}\Delta x = h_s\left[T_w - T_e - r_c u_e^2/(2C_a)\right]\Delta x$$

$$q_{sk}\Delta x = q_{\text{ht}}\Delta x \qquad \text{(for an electrothermal system)}$$

$$= q_{\text{ha}}\Delta x \qquad \text{(for a hot-air system)} \qquad (8b)$$

where i_w is the enthalpy of water and expressed by

$$i_w[T_w(x)] = C_w[T_w(x) - T_{\text{ref}}]$$

$$i_w[T_w(x+\Delta x)] = C_w[T_w(x+\Delta x) - T_{\text{ref}}] \tag{8c}$$

When an electrothermal system is assumed, dividing Eq. (8a) by Δx and using Eqs. (8b) and (8c), we obtain

$$q_{\text{ht}} - h_s\left[T_w - T_e - r_c u_e^2/(2C_a)\right] + \dot{m}''_{\text{imp}}\left[C_w(T_\infty - T_{\text{ref}}) + u_\infty^2/2\right] - F\dot{m}''_{\text{evap}}[C_w(T_w - T_{\text{ref}}) + L_v] - C_w\,\mathrm{d}[\dot{m}'(T_w - T_{\text{ref}})]/\mathrm{d}x = 0 \tag{9a}$$

where the first term of Eq. (9a) represents the heating rate from inside of the skin, the second term the convective heating rate from the surface to the outer flow, the third term the energy rate from the water droplets impinged on the surface, and the fourth term the energy rate lost from the runback water due to evaporation on the surface. The last term corresponds to the change rate of internal energy of the runback water. Equation (9a) is applicable not only in the direct impingement region, where the surface is fully wetted, but also in the downstream region, where $\dot{m}''_{\text{imp}}$ becomes zero and the rivulet flow exists. Splitting $T_\infty - T_{\text{ref}}$ into $T_\infty - T_w + T_w - T_{\text{ref}}$ in the third term of Eq. (9a) and rearranging terms by using Eqs. (1–3), we obtain

$$q_{\text{ht}} - h_s\left[T_w - T_e - \frac{r_c u_e^2}{2C_a}\right] + \dot{m}''_{\text{imp}}\left[C_w(T_\infty - T_w) + \frac{u_\infty^2}{2}\right] - F\dot{m}''_{\text{evap}}L_v - C_w\int_0^x (\dot{m}''_{\text{imp}} - F\dot{m}''_{\text{evap}})\,\mathrm{d}x\frac{\mathrm{d}T_w}{\mathrm{d}x} = 0 \tag{9b}$$

L_v in Eq. (9b) is expressed by[7] $L_v = L_a - L_b T_w$ (where T_w is in kelvin), where L_a is the main part of L_v. This relation was developed by a curve fit to information prepared by the Society of Automotive Engineers.[5] Dividing Eq. (9b) by $-q_{\text{ht},m}$ and using dimensionless parameters, we obtain

$$\int_0^{x^*} \dot{m}''^*_{\text{imp}}\,\mathrm{d}x^*\frac{\mathrm{d}T_w^*}{\mathrm{d}x^*} - \alpha\frac{C_w}{C_a}\int_0^{x^*} Fh_{sr}W_r\,\mathrm{d}x^*\frac{\mathrm{d}T_w^*}{\mathrm{d}x^*} + \alpha F h_{sr}W_r L_v^* + \alpha h_{sr}\left(T_w^* - T_e^* - f^*\right) - \dot{m}''^*_{\text{imp}}\left(T_\infty^* - T_w^* + g^*\right) - q_{\text{htr}} = 0 \tag{9c}$$

where α, $\dot{m}''^*_{\text{imp}}$, and q_{htr} are $h_{s,m}\Delta T_1/q_{\text{ht},m}$, $\dot{m}''_{\text{imp}}C_w\Delta T_1/q_{\text{ht},m}$, and $q_{\text{ht}}/q_{\text{ht},m}$, respectively, and W_r is expressed by

$$W_r = \left(\frac{Pr}{Sc}\right)^{\frac{2}{3}}_{\text{air}}\frac{M_{\text{water}}}{M_{\text{air}}}\left[\frac{P_{v,w} - P_{\text{vap}}}{P_e - P_{v,w}}\right] \tag{10a}$$

$$= \varphi_{\text{evap}}W_{pr} \tag{10b}$$

where

$$W_{pr} = (P_{v,w} - P_{\text{vap}})/(P_e - P_{v,w}) \tag{10c}$$

Equation (3) becomes

$$\dot{m}'^* = \int_0^{x^*}\left(\dot{m}''^*_{\text{imp}} - F\dot{m}''^*_{\text{evap}}\right)\mathrm{d}x^* \tag{11a}$$

$$= \int_0^{x^*}\dot{m}''^*_{\text{imp}}\,\mathrm{d}x^* - \alpha\frac{C_w}{C_a}\int_0^{x^*}Fh_{sr}W_r\,\mathrm{d}x^* \tag{11b}$$

where $\dot{m}'^*$ and $\dot{m}''^*_{\text{evap}}$ are $\dot{m}'\,C_w\Delta T_1/(q_{\text{ht},m}c)$ and $\dot{m}''_{\text{evap}}C_w\Delta T_1/q_{\text{ht},m}$, respectively. Equations (11a) and (11b) express the water mass balance.

Equation (9c) has two nonlinear terms, the second and the third terms, both of which include α explicitly. Basically, assuming that α is small, we can obtain T_w^* and $\dot{m}'^*$ from Eqs. (9c), (11a), and (11b) using the perturbation method. However, the third term is relatively large because the latent heat of evaporation of water, L_v^*, has a large value. It seems to be undesirable from the viewpoint of convergence characteristics of the solution that the nonlinear term takes a large value. In the following development, to improve the convergence properties of the solution, the splitting of the nonlinear term into linear and nonlinear terms is performed and the basic equation for a modified perturbation method is obtained.

Assume $P_{v,w}/P_e$ is small. [If the temperature T_w is relatively low, for example, $T_w = 273{-}303$ K (0–30°C), this assumption would usually be true.] Then we obtain the following relation for W_{pr}:

$$W_{pr} = (P_{v,w} - P_{\text{vap}})/(P_e - P_{v,w}) \cong (P_{v,w} - P_{\text{vap}})/P_e \tag{12a}$$

As the value of $P_{v,w}/P_e$ decreases, W_{pr} also decreases, which reduces the contribution of the nonlinearity in the energy equation.

Assuming that P_e does not change much along the surface, that is, $|1 - P_e/P_{e,m}|$ is small or $P_e/P_{e,m} \cong 1$, we obtain

$$(P_{v,w} - P_{\text{vap}})/P_e \cong (P_{v,w} - P_{\text{vap}})/P_{e,m} \tag{12b}$$

For example, assuming that $T_\infty = -10$°C, $u_\infty = 100$ m/s, and the pressure coefficient C_p changes from 1.0 to −2.0, we can show by a simple calculation that $P_e/P_{e,m}$ takes a value of 1.0, 0.876, and 0.814, for $C_p = 1.0$ (stagnation), −1.0, and −2.0, respectively. These values of $P_e/P_{e,m}$ would conform to the preceding assumption of P_e.

$P_{v,w}$ can be expressed by

$$P_{v,w} = aT_w + b + (P_{v,w} - aT_w - b) \tag{13}$$

where $aT_w + b$ approximates $P_{v,w}$ in a limited region of T_w. If the approximation is good, $|P_{v,w} - aT_w - b|$ may be small compared with a value of $P_{v,w}$ or $aT_w + b$. In Fig. 2, the curve of $P_{v,w}$ based on Eq. (7) and three different approximation lines are shown. The coefficients a and b of each line are 120.87 Pa/K and -3.2403×10^4 Pa, 180.19 Pa/K and -4.8597×10^4 Pa, and 319.89 Pa/K and -8.6766×10^4 Pa. In this paper, the line with $a = 120.87$ Pa/K and $b = -3.2403 \times 10^4$ Pa will mainly be used because this line is nearest to the curve of $P_{v,w}$ with the temperature from about 0°C to about 30°C, the range of concern in the present study.

Substituting Eq. (13) into Eq. (12b) and using Eq. (12a), we obtain

$$W_{pr} \cong [aT_w + b - P_{\text{vap}} + (P_{v,w} - aT_w - b)]/P_{e,m} \tag{14}$$

Because $|P_{v,w} - aT_w - b|$ is small, $(aT_w + b - P_{\text{vap}})/P_{e,m}$ is considered to take a great part of W_{pr}, which is written as

$$W_{pr} = W_{pr1} + W_{pr2} \tag{15}$$

where

$$W_{pr1} = (aT_w + b - P_{\text{vap}})/P_{e,m} \tag{16}$$

$$W_{pr2} = (P_{v,w} - P_{\text{vap}})/(P_e - P_{v,w}) - (aT_w + b - P_{\text{vap}})/P_{e,m} \tag{17}$$

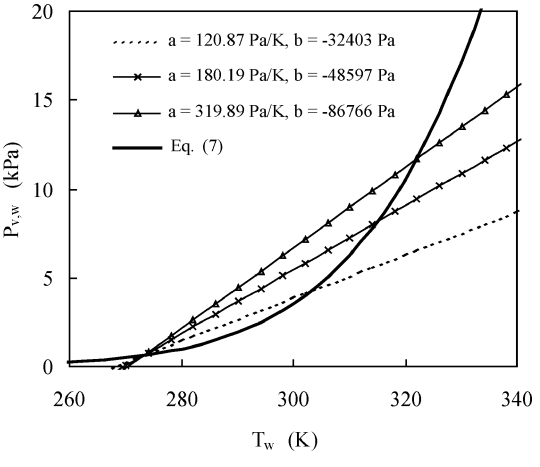

Fig. 2 Approximation of $P_{v,w}$ with lines.

If $P_{v,w}/P_e$ and $|1-P_e/P_{e,m}|$ are small, and the approximation of $P_{v,w}$ with aT_w+b is good, the magnitude of W_{pr2} becomes small compared with that of W_{pr} or W_{pr1}. Substituting Eq. (15) into the third term of Eq. (9c) yields

$$\alpha F h_{sr} W_r L_v^* = \alpha\varphi_{\text{evap}} F h_{sr} W_{pr1} L_v^* + \alpha\varphi_{\text{evap}} F h_{sr} W_{pr2} L_v^* \quad (18a)$$

$$= \alpha\varphi_{\text{evap}} F h_{sr} W_{pr1} L_a^* - \alpha\varphi_{\text{evap}} F h_{sr} W_{pr1} L_b^* T_w^* + \alpha\varphi_{\text{evap}} F h_{sr} W_{pr2} L_v^* \quad (18b)$$

The first term of Eq. (18b) is linear with respect to T_w^* and has a relatively large value. Other terms of Eq. (18b) are nonlinear with relatively small values. Replacing α by ε in the first term of Eq. (18b) yields

$$\alpha F h_{sr} W_r L_v^* = \varepsilon\varphi_{\text{evap}} F h_{sr} W_{pr1} L_a^* - \alpha\varphi_{\text{evap}} F h_{sr} W_{pr1} L_b^* T_w^* + \alpha\varphi_{\text{evap}} F h_{sr} W_{pr2} L_v^* \quad (19)$$

Substituting Eq. (19) into Eq. (9c) by using Eqs. (16) and (17), and replacing α by ε in the fourth term of Eq. (9c), we obtain the energy balance equation for the modified perturbation method, which is written as

$$\int_0^{x^*} \dot{m}_{\text{imp}}'^* \,\mathrm{d}x^* \frac{\mathrm{d}T_w^*}{\mathrm{d}x^*} - \alpha\frac{C_w}{C_a}\int_0^{x^*} F h_{sr} W_r \,\mathrm{d}x^* \frac{\mathrm{d}T_w^*}{\mathrm{d}x^*} + \varepsilon\varphi_{\text{evap}} F h_{sr} \times \left(\frac{a\Delta T_1 T_w^* + b - P_{\text{vap}}}{P_{e,m}}\right) L_a^* - \alpha\varphi_{\text{evap}} F h_{sr}\left(\frac{a\Delta T_1 T_w^* + b - P_{\text{vap}}}{P_{e,m}}\right) \times L_b^* T_w^* + \alpha\varphi_{\text{evap}} F h_{sr}\left(\frac{W_r}{\varphi_{\text{evap}}} - \frac{a\Delta T_1 T_w^* + b - P_{\text{vap}}}{P_{e,m}}\right) L_v^* + \varepsilon h_{sr}\left(T_w^* - T_e^* - f^*\right) - \dot{m}_{\text{imp}}'^*\left(T_\infty^* - T_w^* + g^*\right) - q_{\text{htr}} = 0 \quad (20)$$

The first and second terms of Eq. (20) become zero at $x^*=0$, which gives the boundary condition.

Equations (9a–20) for an electrothermal anti-icing system are also applicable to a hot-air anti-icing system, when some parameters are defined or replaced,

$$q_{\text{ht}} \to q_{\text{ha}} (q_{\text{ht}} \text{ is replaced by } q_{\text{ha}})$$

$$q_{\text{htr}} \to q_{\text{har}} (q_{\text{htr}} \text{ is replaced by } q_{\text{har}})$$

$$\dot{m}'^* = \dot{m}' C_w \Delta T_1/(h_{\text{ha},m}\Delta T_2 c)$$

$$\dot{m}_{\text{imp}}'^* = \dot{m}_{\text{imp}}'' C_w \Delta T_1/(h_{\text{ha},m}\Delta T_2)$$

$$\dot{m}_{\text{evap}}'^* = \dot{m}_{\text{evap}}'' C_w \Delta T_1/(h_{\text{ha},m}\Delta T_2)$$

$$\alpha = h_{s,m}\Delta T_1/(h_{\text{ha},m}\Delta T_2) \quad (21)$$

Analytical Solution Based on a Modified Perturbation Method

A. Solution for an Electrothermal Anti-icing System

Assuming that α is small, we may express the solution of Eq. (20), T_w^*, as a power series in α, which is written as

$$T_w^* = T_{w0}^* + \alpha T_{w1}^* + \alpha^2 T_{w2}^* + \alpha^3 T_{w3}^* + \cdots \quad (22)$$

Substituting Eq. (22) into Eq. (10a) yields

$$W_r\left(T_w^*, x^*\right) = W_r\left(T_{w0}^* + \alpha T_{w1}^* + \alpha^2 T_{w2}^* + \cdots, x^*\right) \quad (23)$$

Expanding $W_r(T_w^*, x^*)$ in powers of α gives the Maclaurin series, which is given by

$$W_r\left(T_w^*, x^*\right) = (W_r)_{\alpha=0} + \alpha\left(\frac{\mathrm{d}W_r}{\mathrm{d}\alpha}\right)_{\alpha=0} + \left(\frac{\alpha^2}{2}\right)\left(\frac{\mathrm{d}^2 W_r}{\mathrm{d}\alpha^2}\right)_{\alpha=0} + \cdots \quad (24)$$

where

$$(W_r)_{\alpha=0} = W_r\left(T_{w0}^*, x^*\right)$$

$$\left(\frac{\mathrm{d}W_r}{\mathrm{d}\alpha}\right)_{\alpha=0} = \left(\frac{\mathrm{d}T_w^*}{\mathrm{d}\alpha}\right)_{\alpha=0}\left(\frac{\partial W_r}{\partial T_w^*}\right)_{\alpha=0} = T_{w1}^*\left(\frac{\partial W_r}{\partial T_w^*}\right)_{\alpha=0}$$

$$\left(\frac{\mathrm{d}^2 W_r}{\mathrm{d}\alpha^2}\right)_{\alpha=0} = \left(\frac{\mathrm{d}^2 T_w^*}{\mathrm{d}\alpha^2}\right)_{\alpha=0}\left(\frac{\partial W_r}{\partial T_w^*}\right)_{\alpha=0} + \left(\frac{\mathrm{d}T_w^*}{\mathrm{d}\alpha}\right)_{\alpha=0}\left(\frac{\mathrm{d}T_w^*}{\mathrm{d}\alpha}\right)_{\alpha=0}\left(\frac{\partial^2 W_r}{\partial T_w^{*2}}\right)_{\alpha=0} = 2T_{w2}^*\left(\frac{\partial W_r}{\partial T_w^*}\right)_{\alpha=0} + T_{w1}^{*2}\left(\frac{\partial^2 W_r}{\partial T_w^{*2}}\right)_{\alpha=0} \quad (25)$$

Substituting Eq. (25) into Eq. (24) yields

$$W_r\left(T_w^*, x^*\right) = W_r\left(T_{w0}^*, x^*\right) + \alpha T_{w1}^*\frac{\partial W_r}{\partial T_w^*} + \frac{1}{2}\alpha^2\left(2T_{w2}^*\frac{\partial W_r}{\partial T_w^*} + T_{w1}^{*2}\frac{\partial^2 W_r}{\partial T_w^{*2}}\right) + \cdots \quad (26)$$

where $\partial W_r/\partial T_w^*$ and $\partial^2 W_r/\partial T_w^{*2}$ are $\partial W_r(T_{w0}^*, x^*)/\partial T_w^*$ and $\partial^2 W_r(T_{w0}^*, x^*)/\partial T_w^{*2}$, respectively.

Substituting Eq. (22) into Eq. (20) by using Eq. (26), summing the coefficients of like powers of α, and setting them to zero, we obtain the following relations. (In this paper, the equation and solution corresponding to the coefficient of α^i is called the ith-order equation and solution, respectively. In the following development, W_r, W_{pr}, and $\partial W_r/\partial T_w^* \cdots$ mean $W_r(T_{w0}^*, x^*)$, $W_{pr}(T_{w0}^*, x^*)$, and $\partial W_r(T_{w0}^*, x^*)/\partial T_w^* \cdots$).

1. *Zeroth-Order Equation and Solution*

$$G_0(x^*)\frac{\mathrm{d}T_{w0}^*}{\mathrm{d}x^*} + H_0(x^*)T_{w0}^* + I_0(x^*) = 0 \quad (27)$$

where

$$G_0(x^*) = \int_0^{x^*} \dot{m}_{\text{imp}}'^* \,\mathrm{d}x^*, \qquad H_0(x^*) = H_{01}(x^*) + \varepsilon H_{02}(x^*)$$

$$H_{01}(x^*) = \dot{m}_{\text{imp}}'^*, \qquad H_{02}(x^*) = F\varphi_{\text{evap}} h_{sr}\left(\frac{a\Delta T_1}{P_{e,m}}\right)L_a^* + h_{sr}$$

$$I_0(x^*) = I_{01}(x^*) + \varepsilon I_{02}(x^*), \qquad I_{01}(x^*) = -\dot{m}_{\text{imp}}'^*\left(T_\infty^* + g^*\right) - q_{\text{htr}}$$

$$I_{02}(x^*) = F\varphi_{\text{evap}} h_{sr}\left(\frac{b - P_{\text{vap}}}{P_{e,m}}\right)L_a^* - h_{sr}\left(T_e^* + f^*\right) \quad (28)$$

The boundary condition at $x^*=0$ is written as

$$H_0(0)T_{w0}^*(0) + I_0(0) = 0 \quad (29)$$

The solution of Eq. (27) is given by

$$T_{w0}^*(x^*) = A_0(x^*)\left[-\int_0^{x^*} \bar{I}_0(x^*)B_0(x^*)\,\mathrm{d}x^* + C_0\right]$$

$$A_0(x^*) = \exp\left[-\int_0^{x^*} \bar{H}_0(x^*)\,\mathrm{d}x^*\right]$$

$$B_0(x^*) = \exp\left[\int_0^{x^*} \bar{H}_0(x^*)\,\mathrm{d}x^*\right]$$

$$C_0 = -\frac{I_0(0)}{H_0(0)}, \qquad \bar{I}_0 = \frac{I_0(x^*)}{G_0(x^*)}, \qquad \bar{H}_0 = \frac{H_0(x^*)}{G_0(x^*)} \quad (30)$$

2. First-Order Equation and Solution

$$G_0(x^*)\frac{\mathrm{d}T^*_{w1}}{\mathrm{d}x^*} + H_0(x^*)T^*_{w1} + I_1(x^*) = 0 \tag{31}$$

where

$$I_1(x^*) = I_{11}(x^*) + I_{12}(x^*) + I_{13}(x^*)$$

$$I_{11}(x^*) = -\frac{C_w}{C_a}\int_0^{x^*} Fh_{sr}W_r\,\mathrm{d}x^*\frac{\mathrm{d}T^*_{w0}}{\mathrm{d}x^*}$$

$$I_{12}(x^*) = -\varphi_{\mathrm{evap}}Fh_{sr}\left(\frac{a\Delta T_1 T^*_{w0} + b - P_{\mathrm{vap}}}{P_{e,m}}\right)L^*_b T^*_{w0}$$

$$I_{13}(x^*) = \varphi_{\mathrm{evap}}Fh_{sr}\left(W_{pr} - \frac{a\Delta T_1 T^*_{w0} + b - P_{\mathrm{vap}}}{P_{e,m}}\right)\left(L^*_a - L^*_b T^*_{w0}\right) \tag{32}$$

The boundary condition at $x^* = 0$ is written as

$$H_0(0)T^*_{w1}(0) + I_1(0) = 0 \tag{33}$$

The solution of Eq. (31) is given by

$$T^*_{w1}(x^*) = A_0(x^*)\left[-\int_0^{x^*}\bar{I}_1(x^*)B_0(x^*)\,\mathrm{d}x^* + C_1\right]$$

$$C_1 = -\frac{I_1(0)}{H_0(0)}, \qquad \bar{I}_1 = \frac{I_1(x^*)}{G_0(x^*)} \tag{34}$$

3. Second-Order Equation and Solution

$$G_0(x^*)\frac{\mathrm{d}T^*_{w2}}{\mathrm{d}x^*} + H_0(x^*)T^*_{w2} + I_2(x^*) = 0 \tag{35}$$

where

$$I_2(x^*) = I_{21}(x^*) + I_{22}(x^*) + I_{23}(x^*) + I_{24}(x^*) + I_{25}(x^*)$$

$$I_{21}(x^*) = -\frac{C_w}{C_a}\int_0^{x^*} Fh_{sr}W_r\,\mathrm{d}x^*\frac{\mathrm{d}T^*_{w1}}{\mathrm{d}x^*}$$

$$I_{22}(x^*) = -\frac{C_w}{C_a}\int_0^{x^*} Fh_{sr}T^*_{w1}\frac{\partial W_r}{\partial T^*_w}\,\mathrm{d}x^*\frac{\mathrm{d}T^*_{w0}}{\mathrm{d}x^*}$$

$$I_{23}(x^*) = -\varphi_{\mathrm{evap}}Fh_{sr}\left(\frac{a\Delta T_1}{P_{e,m}}\right)L^*_b T^*_{w0}T^*_{w1}$$

$$I_{24}(x^*) = -\varphi_{\mathrm{evap}}Fh_{sr}W_{pr}L^*_b T^*_{w1}$$

$$I_{25}(x^*) = \varphi_{\mathrm{evap}}Fh_{sr}\left(T^*_{w1}\frac{\partial W_{pr}}{\partial T^*_w} - \frac{a\Delta T_1 T^*_{w1}}{P_{e,m}}\right)\left(L^*_a - L^*_b T^*_{w0}\right) \tag{36}$$

The boundary condition at $x^* = 0$ is written as

$$H_0(0)T^*_{w2}(0) + I_2(0) = 0 \tag{37}$$

The solution of Eq. (35) is given by

$$T^*_{w2}(x^*) = A_0(x^*)\left[-\int_0^{x^*}\bar{I}_2(x^*)B_0(x^*)\,\mathrm{d}x^* + C_2\right]$$

$$C_2 = -\frac{I_2(0)}{H_0(0)}, \qquad \bar{I}_2 = \frac{I_2(x^*)}{G_0(x^*)} \tag{38}$$

4. Third-Order Equation and Solution

$$G_0(x^*)\frac{\mathrm{d}T^*_{w3}}{\mathrm{d}x^*} + H_0(x^*)T^*_{w3} + I_3(x^*) = 0 \tag{39}$$

where

$$I_3(x^*) = \sum_{i=1}^{7} I_{3i}(x^*), \qquad I_{31}(x^*) = -\frac{C_w}{C_a}\int_0^{x^*} Fh_{sr}W_r\,\mathrm{d}x^*\frac{\mathrm{d}T^*_{w2}}{\mathrm{d}x^*}$$

$$I_{32}(x^*) = -\frac{C_w}{C_a}\int_0^{x^*} Fh_{sr}T^*_{w1}\frac{\partial W_r}{\partial T^*_w}\,\mathrm{d}x^*\frac{\mathrm{d}T^*_{w1}}{\mathrm{d}x^*}$$

$$I_{33}(x^*) = -\frac{C_w}{C_a}\int_0^{x^*} Fh_{sr}\left(T^*_{w2}\frac{\partial W_r}{\partial T^*_w} + \frac{1}{2}T^{*2}_{w1}\frac{\partial^2 W_r}{\partial T^{*2}_w}\right)\mathrm{d}x^*\frac{\mathrm{d}T^*_{w0}}{\mathrm{d}x^*}$$

$$I_{34}(x^*) = \varphi_{\mathrm{evap}}Fh_{sr}T^*_{w1}\frac{\partial W_{pr}}{\partial T^*_w}\left(-L^*_b T^*_{w1}\right)$$

$$I_{35}(x^*) = \varphi_{\mathrm{evap}}Fh_{sr}\left(T^*_{w2}\frac{\partial W_{pr}}{\partial T^*_w} + \frac{1}{2}T^{*2}_{w1}\frac{\partial^2 W_{pr}}{\partial T^{*2}_w}\right)\left(L^*_a - L^*_b T^*_{w0}\right)$$

$$I_{36}(x^*) = -\varphi_{\mathrm{evap}}Fh_{sr}\left(\frac{a\Delta T_1 T^*_{w2}}{P_{e,m}}\right)L^*_a$$

$$I_{37}(x^*) = -\varphi_{\mathrm{evap}}Fh_{sr}W_{pr}L^*_b T^*_{w2} \tag{40}$$

The boundary condition at $x^* = 0$ is written as

$$H_0(0)T^*_{w3}(0) + I_3(0) = 0 \tag{41}$$

The solution of Eq. (39) is given by

$$T^*_{w3}(x^*) = A_0(x^*)\left[-\int_0^{x^*}\bar{I}_3(x^*)B_0(x^*)\,\mathrm{d}x^* + C_3\right]$$

$$C_3 = -\frac{I_3(0)}{H_0(0)}, \qquad \bar{I}_3 = \frac{I_3(x^*)}{G_0(x^*)} \tag{42}$$

Substituting Eq. (22) into Eq. (11b) and using Eqs. (23–26), we obtain $\dot{m}'^*$ expressed in a series in powers of α as follows:

$$\dot{m}'^* = \dot{m}'^*_0 + \alpha\dot{m}'^*_1 + \alpha^2\dot{m}'^*_2 + \alpha^3\dot{m}'^*_3 + \cdots \tag{43}$$

where

$$\dot{m}'^*_0 = G_0(x^*) = \int_0^{x^*}\dot{m}''^*_{\mathrm{imp}}\,\mathrm{d}x^*, \qquad \dot{m}'^*_1 = -\frac{C_w}{C_a}\int_0^{x^*} Fh_{sr}W_r\,\mathrm{d}x^*$$

$$\dot{m}'^*_2 = -\frac{C_w}{C_a}\int_0^{x^*} Fh_{sr}T^*_{w1}\frac{\partial W_r}{\partial T^*_w}\,\mathrm{d}x^*$$

$$\dot{m}'^*_3 = -\frac{C_w}{C_a}\int_0^{x^*} Fh_{sr}\left(T^*_{w2}\frac{\partial W_r}{\partial T^*_w} + \frac{1}{2}T^{*2}_{w1}\frac{\partial^2 W_r}{\partial T^{*2}_w}\right)\mathrm{d}x^* \tag{44}$$

B. Solution for a Hot-Air Anti-icing System

Equations (22–44) and the relevant discussions for the solution for an electrothermal anti-icing system are also applicable to the solution for a hot-air anti-icing system if $H_{01}(x^*)$ and $I_{01}(x^*)$ in Eq. (28) are replaced according to Eq. (45) and parameters are defined according to Eq. (21):

$$H_{01}(x^*) = \dot{m}''^*_{\mathrm{imp}} + h_{\mathrm{har}}\Delta T_1/\Delta T_2$$

$$I_{01}(x^*) = -\dot{m}''^*_{\mathrm{imp}}\left(T^*_\infty + g^*\right) - h_{\mathrm{har}}(\Delta T_1/\Delta T_2)T^*_{\mathrm{hotair}} \tag{45}$$

Analytical and Numerical Solutions

Several examples are described to demonstrate the characteristics of the analytical solution presented. (In the following subsections, except when specifically mentioned, the approximation line with $a = 120.87$ Pa/K and $b = -30403$ Pa is used for the calculation of the analytical solution.)

A. Electrothermal Anti-icing System

Consider liquid water droplets impinging on the leading edge of an airfoil surface such that the distribution of the water impingement is as shown in Fig. 3. The airfoil skin is made out of metal and is assumed to be fitted with an electrothermal ice protection system at the leading edge. Flow conditions for the calculation are taken to be $V_\infty = 44.7$ m/s, $P_\infty = 1.0 \times 10^5$ Pa, $T_\infty = 265.5$ K, and LWC $= 0.78 \times 10^{-3}$ kg/m^3. These values are based on the anti-icing experiments[17] on a NACA0012 airfoil model of 0.9144-m (36-in.) chord length. (P_∞ is a roughly estimated value by the author based on the experiment.[17]) The assumed external heat transfer coefficient is shown in Fig. 4. For $0 \le x \le 0.0792$ m, the curve is based on the data of the laminar heat transfer coefficient obtained experimentally in a dry flow condition.[17] For x greater than 0.0792 m, experimental data are not available, and a constant value of 70.19 W/m$^2 \cdot$K is assumed. The pressure coefficient used is based on the calculated value[11] for a NACA0012 airfoil and is shown in Fig. 5.

The surface temperature solutions at various orders for an electrothermal anti-icing system are shown in Fig. 6, where the heating rate is assumed to be a constant value of 4000 W/m^2 and $F = 1$. In Fig. 6, the surface temperature obtained by the fourth-order Runge–Kutta method in Eq. (9c) is also shown for comparison. It is seen that the temperature solutions of second and third order agree well with the numerical solution, which suggests that, as the order of the solution increases, it approaches an exact solution. The

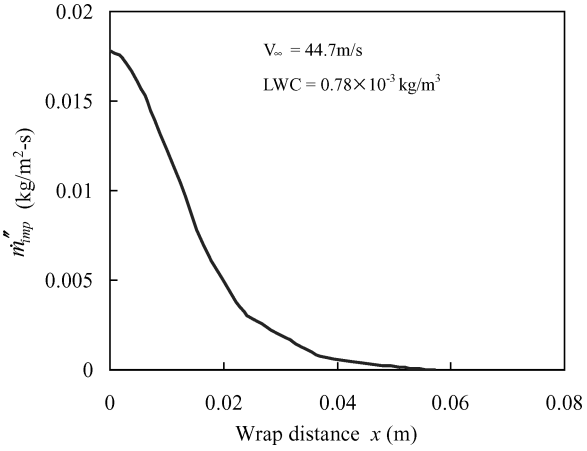

Fig. 3 Rate of water impingement per unit area.

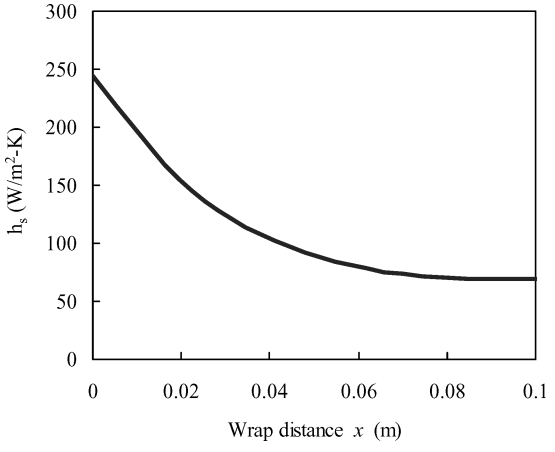

Fig. 4 External heat transfer coefficient h_s.

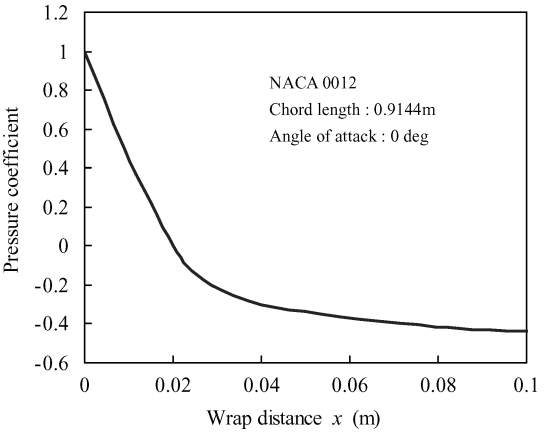

Fig. 5 Pressure coefficient.

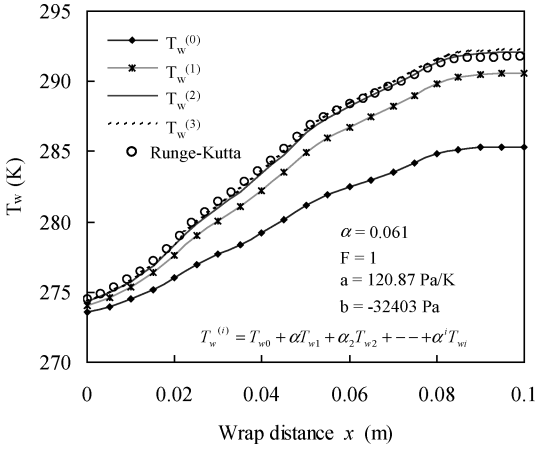

Fig. 6 Temperature solutions at various orders compared with numerical result of Runge–Kutta method.

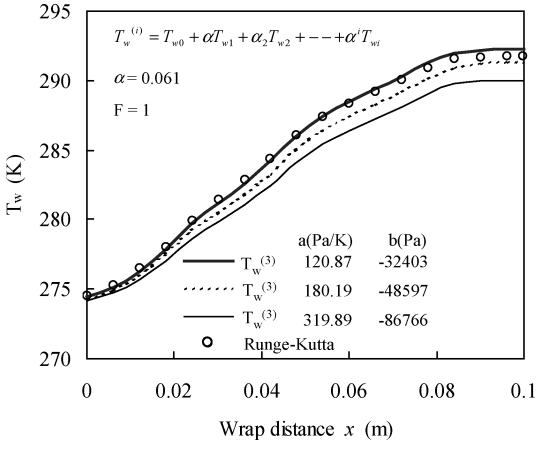

Fig. 7 Effect of approximation lines on surface temperature.

effect of the approximation lines of $P_{v,w}$ on T_w is shown in Fig. 7, where the approximation lines are defined in Fig. 2. It is seen that the line with $a = 120.87$ Pa/K and $b = -3.0403 \times 10^4$ Pa gives the most accurate solution among the lines, as is obvious from Fig. 2. Figure 8 shows the zeroth- to third-order solutions of $\dot{m}'$ and a numerical solution obtained by the Runge–Kutta method. As with T_w, the solutions of at least second and third order agree well with the numerical solution, which suggests that as the order of the solution increases, it approaches an exact solution. The effect of the heating rate $q_{\mathrm{ht},m}$ on the third-order surface temperature solutions is shown in Fig. 9, where each $q_{\mathrm{ht},m}$ takes a constant value of 4000, 6000, and 8000 W/m^2, respectively. Solutions obtained by the Runge–Kutta

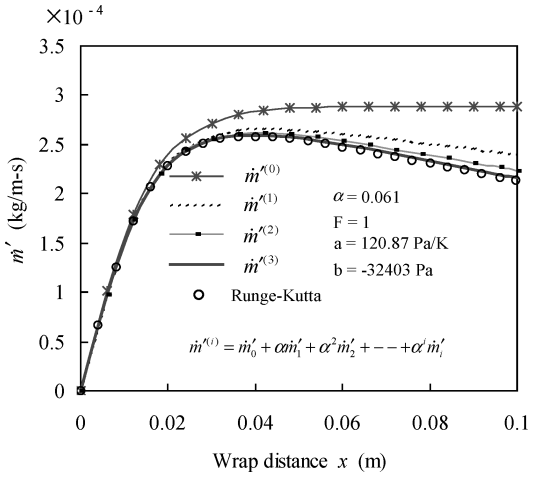

Fig. 8 Mass flow rate solutions at various orders compared with numerical result of Runge–Kutta method.

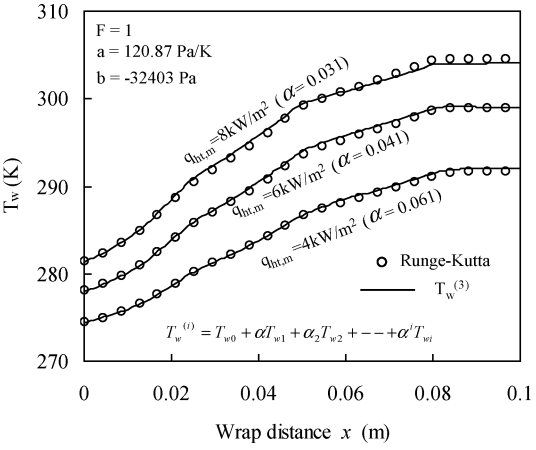

Fig. 9 Effect of heating rate $q_{\mathrm{ht},m}$ on the surface temperature solutions.

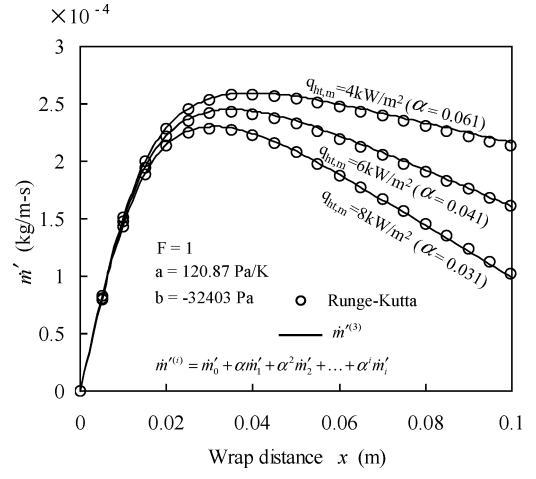

Fig. 10 Effect of heating rate $q_{\mathrm{ht},m}$ on mass flow rate solutions.

method are also shown for comparison. The third-order solution $T_w^{(3)}$ with $q_{\mathrm{ht},m} = 4000$ W/m^2 in Fig. 9 is the same as the third-order solution $T_w^{(3)}$ in Fig. 6. It is seen that the surface temperature increases as $q_{\mathrm{ht},m}$ increases and the third-order solutions agree very well with the corresponding numerical solutions. Figure 10 shows the third-order water mass flow rate solutions with the corresponding numerical solutions. When x is small, the three water mass flow rate solutions increase as x increases and have almost the same values. When x is large, the water mass flow rate solutions decrease as x increases. The level of decrease becomes much higher when $q_{\mathrm{ht},m}$ increases. In

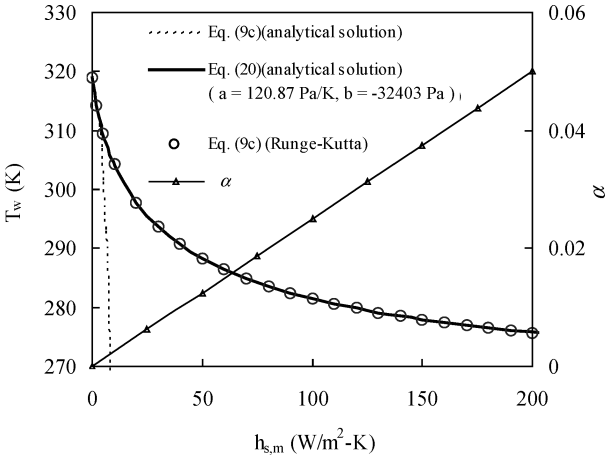

Fig. 11 Effect of external heat transfer coefficient on solutions of surface temperature (stagnation point).

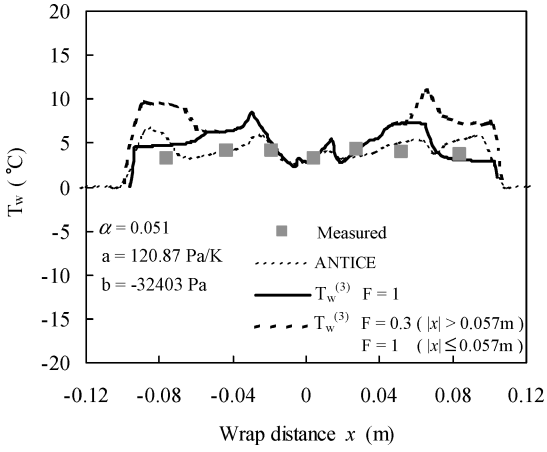

Fig. 12 Surface temperature solution of third order compared with measured data and ANTICE result.

a similar way to the surface temperature solutions, the third-order water mass flow rate solutions agree very well with the numerical solutions.

Figure 11 shows the effect of the external heat transfer coefficient $h_{s,m}$ on the surface temperature at stagnation. Three kinds of solutions are shown in Fig. 11. One is the third-order analytical solution of Eq. (20), where splitting of the latent heat term into linear and nonlinear terms and the use of the parameter ε are implemented. Another is a numerical solution of Eq. (9c) by the Runge–Kutta method. The third is the third-order solution obtained by substituting Eq. (22) into Eq. (9c) and equating the coefficients of like powers of α, where splitting of the latent heat term and the use of ε are not implemented. The perturbation parameter α is also shown in Fig. 11. There is only a slight difference between the third-order solution of Eq. (20) and the numerical solution of Eq. (9c). The third order solution of Eq. (9c) agrees well with the other solutions only when $h_{s,m}$ is less than about 5 W/m$^2 \cdot$K, which corresponds to extremely small $\alpha(= 0.001)$. The differences increase sharply as $h_{s,m}$ increases. This means that the analytical solution of Eq. (9c) is virtually impossible for practical applications. On the other hand, the analytical solution of Eq. (20), which is presented in this paper, would be very useful for practical applications.

Here, another example of the analytical solution is described. Figure 12 shows the calculation result of T_w together with the anti-icing experimental results and the numerical result of the ANTICE code.[17] Figure 13 shows the calculation result of the water mass flow rate in comparison with the numerical result of the ANTICE code.[17] The anti-icing experimental results[17] were obtained on a NACA0012 airfoil model of 0.9144-m (36-in.) chord length fitted with an electrothermal ice protection system at the leading edge.

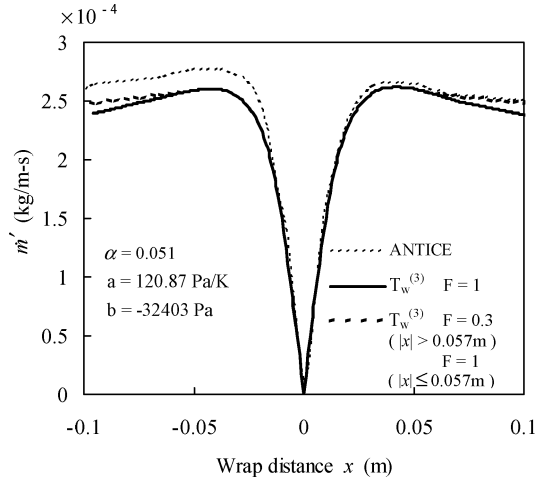

Fig. 13 Mass flow rate solution of third order compared with calculation result of ANTICE.

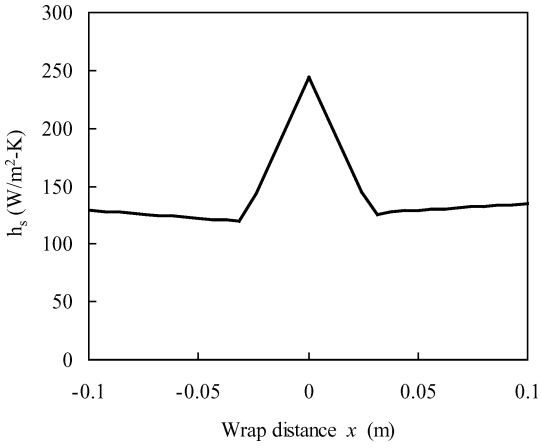

Fig. 14 External heat transfer coefficient h_s.

Parameters for the calculation are set according to the running-wet anti-icing test case of 22B in Ref. 17. Flow conditions are the same as those used in Figs. 6–11. The rate of water impingement in Fig. 3 and the pressure coefficient in Fig. 5 are used for the calculation, in which each of these values at point x is considered to be the same as that at point $-x$. The external heat transfer coefficient are shown in Fig. 14. When $-0.03175 \le x \le 0.03175$ m ($-1.25 \le x \le 1.25$ in.), the curve in Fig. 14 corresponds to the laminar heat transfer coefficient, which is taken from the measured data of Ref. 17. When $x \le -0.03175$ m (-1.25 in.) or 0.03175 m (1.25 in.) $\le x$, the transition region from the laminar to the turbulent heat transfer is assumed to begin at $x = \pm 0.03175$ m (± 1.25 in.) (Ref. 17) and $h_s(x)$ for the transition region is calculated by the following relation[7]:

$$h_s(x) = h_{s,\text{lamt}} + \frac{Re(x) - Re_{\text{lamt}}}{Re_{\text{turbt}} - Re_{\text{lamt}}}(h_{s,\text{turbt}} - h_{s,\text{lamt}}) \qquad (46)$$

where $Re(x)$ is the Reynolds number at the point x [$Re(x) = u_e x/\nu_a$]; Re_{lamt} and $h_{s,\text{lamt}}$ the Reynolds number and the laminar heat transfer coefficient, respectively, at a transition point ($x = x_{\text{lamt}} = \pm 0.03175$ m); and Re_{turbt} and $h_{s,\text{turbt}}$ the Reynolds number and the turbulent heat transfer coefficient, respectively, at another transition point ($x = x_{\text{turbt}}$), where the transition region ends and fully turbulent flow begins. (For the present calculation, $Re_{\text{turbt}} = 1.2 \times 10^6$ is assumed.[7]) The heat transfer coefficient $h_{s,\text{turbt}}$ at $x = x_{\text{turbt}}$ is given by the expression for the turbulent heat transfer coefficient of a flat plate and is written as[7]

$$h_{s,\text{turbt}} = 0.0296[Re(x_{\text{turbt}})]^{0.8}(Pr)^{\frac{1}{3}}k_a \big/ x_{\text{turbt}} \qquad (47)$$

The electrothermal ice protection system consisted of seven heater bands, three on each side of the airfoil and one approximately centered on the leading edge, as shown in Fig. 15. Table 1 lists the wrap coordinates of each of the heaters and the individual power density used for the present case. The value of the parameter α is 0.051, which is calculated based on the values of $q_{\text{ht},m}$ (= 4805.01 W/m^2) and $h_{s,m}$ (= 244.4 W/m^2 · K) at the stagnation point. The calculation of the solution is performed in the range of x where T_w is greater than 0°C because the heat balance model in the present paper assumes the runback water with the temperature of greater than 0°C. The results of Ref. 17 in about the same range of x are shown for comparison. The wetness factor F is assumed to take a value of unity within the range of water droplet impingement ($-0.057 \le x \le 0.057$ m). Beyond the impingement limits ($x \le -0.057$ m or $0.057 \text{ m} \le x$), F is assumed to take a constant value of 0.3. (For comparison fully wetted case of $F = 1.0$ is also considered.) Figure 12 shows that the third-order surface temperature solution agrees relatively well with the experimental and the numerical results of Ref. 17. Figure 13 shows that the third-order water mass flow rate solution agrees relatively well with the ANTICE result. In the neighborhood of the stagnation point, in the direct impingement region, the surface temperature and the water mass flow rate solutions agree very well with the results of ANTICE. As $|x|$ increases, the surface temperature solution becomes slightly higher than the ANTICE result and the water mass flow rate solution becomes slightly lower than the ANTICE result. When the temperature of the runback water increases, the mass loss rate due to evaporation increases, which is the reason why the mass flow rate solution in Fig. 13 is slightly lower than the ANTICE result. Beyond the impingement limits, the temperature calculated with $F = 0.3$ is larger than the results of Ref. 17. The surface temperature and the water mass flow rate calculated with $F = 0.3$ are larger than those with $F = 1.0$. The reason for this tendency is that the runback water surface area for $F = 0.3$ is smaller than that for $F = 1.0$, which causes the energy loss and the mass loss due to evaporation with $F = 0.3$ to be smaller than that with $F = 1.0$.

Table 1 Wrap position and power density of heater elements

Heater	Start[a] x, m	End[a] x, m	Power density W/m^2
H1	−0.0936[a]	−0.0555	2635.01
H2	−0.0555	−0.0301	2945.01
H3	−0.0301	−0.0047	4030.01
H4	−0.0047	0.0144	4805.01
H5	0.0144	0.0398	2945.00
H6	0.0398	0.0652	3410.01
H7	0.0652	0.1033	2325.00

[a]Negative value of x refers to lower surface.

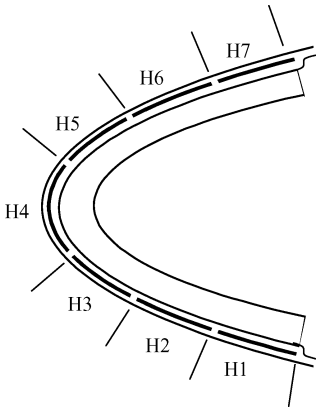

Fig. 15 Heater elements inside airfoil.

B. Hot-Air Anti-icing System

Calculated results of the analytical solution for a hot-air anti-icing system are compared to those of Al-Khalil et al.[10] and Morency et al.[12] Consider liquid water droplets impinging on the leading edge of an airfoil surface. The rate of water impingement per unit area, $\dot{m}''_{\text{imp}}$, is shown in Fig. 16. The surface is assumed to be heated on

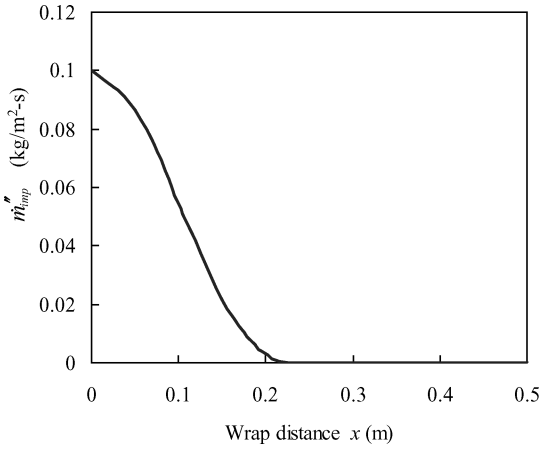

Fig. 16 Rate of water impingement per unit area.

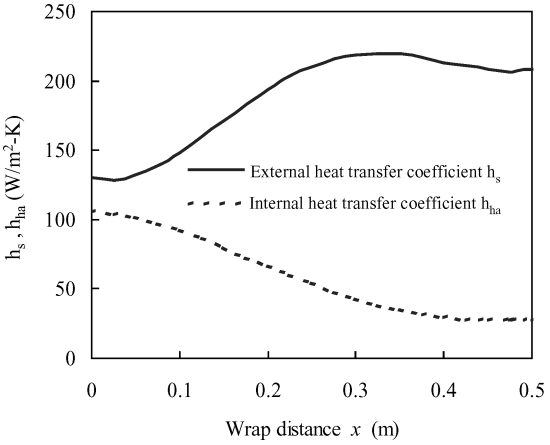

Fig. 17 External and internal heat transfer coefficient.

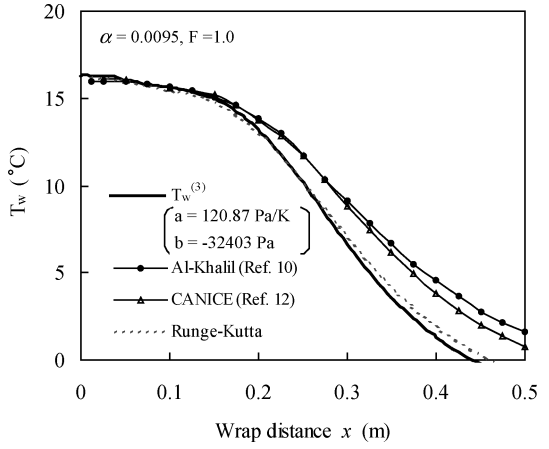

Fig. 18 Calculated surface temperature T_w.

the interior by means of convection from hot air whose temperature varies linearly from 220°C at $x = 0$ m to 120°C at $x = 0.5$ m. The solid wall is a single metal layer and has a thermal conductivity of 100 W/m · K. The external and the internal heat transfer coefficients are shown in Fig. 17. The wetness factor F is assumed to take a constant value of unity. T_∞, P_∞, and Φ_∞ are assumed to be -10°C, 0.5 atm, and 100%, respectively. The calculated result of the surface temperature of third order is shown in Fig. 18 together with the numerical solution by the Runge–Kutta method and other numerical results of Al-Khalil et al.[10] and the CANICE code.[12] These results, except for the third-order solution, were obtained by numerical techniques. It is seen that the third-order solution agrees well with the numerical solution by the Runge–Kutta method. The third-order solution is slightly lower than the results of the other codes, when

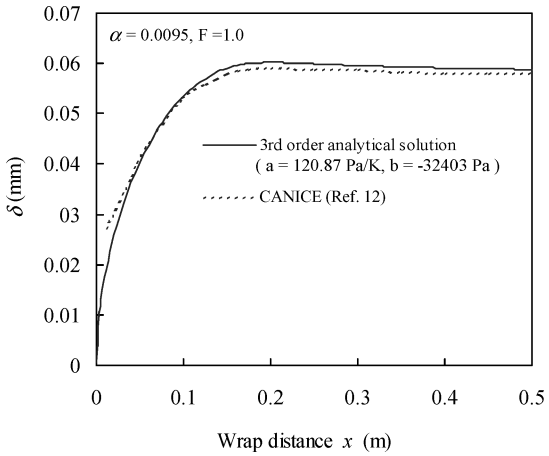

Fig. 19 Calculated water film thickness δ.

x increases. The reason for the deviation of the temperature would probably be due to the differences of each energy model used. These two codes use two-dimensional models for the runback water, and the heat conduction in the skin in the flow direction is also taken into account. In the present study, the one-dimensional model is used, in which the temperature gradient across the thickness of the water and the skin is neglected, and the heat conduction in the flow direction is neglected. In spite of the differences of the models, the third-order solution agrees relatively well with the results of the other codes. The main reasons would be that the temperature variation across the thickness is small[10] (less than about 1°C) and the effect of the heat conduction in the skin along the airflow direction on the temperature is probably not very large. For these reasons, the calculation result based on the one-dimensional model agrees relatively well with the results based on the two-dimensional models. Figure 19 shows the calculated thickness δ of the runback water film together with the result of CANICE.[12] For the calculation of δ, the aerodynamic shear stress τ_a is assumed 10 Pa and the following relation[8] is used:

$$\delta = (2\nu_w \dot{m}'_w/\tau_a)^{\frac{1}{2}} \tag{48}$$

where ν_w is the kinematic viscosity of water. It is seen that the calculated water film thickness agrees well with the result of CANICE.

C. Effectiveness of the Solution

At the least, the solution by the modified perturbation method in this paper would be effective if α is small enough. If the following three conditions are satisfied at the same time, the contribution of the nonlinearity in Eq. (20) would be reduced, which would lead to good convergence properties of the solution.

Condition 1 is that $P_{v,w}/P_e$ is small. [This gives a good approximation of W_{pr} with $(P_{v,w} - P_{\text{vap}})/P_e$ in Eq. (12a) and also contributes to reduce the value of W_{pr} in Eq. (12a).]

Condition 2 is that P_e does not change greatly along the surface. [This gives a good approximation of $(P_{v,w} - P_{\text{vap}})/P_e$ with $(P_{v,w} - P_{\text{vap}})/P_{e,m}$ in Eq. (12b).]

Condition 3 is that $P_{v,w}$ is approximated properly by $aT_w + b$ in a limited range of T_w. [This contributes to reduce the amount of the nonlinear term W_{pr2} in Eq. (15).]

The convergence of the solution may be examined also by introducing a new parameter, r^i, which is given by the following expression:

$$r^i = \left[\left(\sum_{k=1}^{n} E_k^i \right)^2 \Big/ \left(\sum_{k=1}^{n} \left(E_k^i\right)^2 \right) \right]^{\frac{1}{2}} \tag{49}$$

where n is the total number of terms in Eq. (20), $(n = 8)$, and E_k^i is the kth term of Eq. (20) substituted by the ith-order solution $T_w^{*(i)}$, which is given by

$$T_w^{*(i)} = T_{w0}^* + \alpha T_{w1}^* + \alpha^2 T_{w2}^* + \cdots + \alpha^i T_{wi}^* \tag{50}$$

Table 2 Parameter $\bar{r}^i$ for evaluation of convergence

Figure no.	$\bar{r}^i$ for each order solution $T_w^{*(i)}$ $i=0$	$i=1$	$i=2$	$i=3$	α	Remarks[a]
7	0.241	0.066	0.016	0.009	0.061	$a=120.87$ Pa/K, $b=-3.2403$ Pa
7	0.311	0.135	0.055	0.018	0.061	$a=180.19$ Pa/K, $b=-4.8597$ Pa
7	0.387	0.218	0.128	0.078	0.061	$a=319.89$ Pa/K, $b=-8.6766$ Pa
9	0.208	0.053	0.019	0.011	0.031	$q_{ht,m}=8000$ W/m^2
9	0.239	0.043	0.024	0.008	0.041	$q_{ht,m}=6000$ W/m^2
11	0.157	0.065	0.026	0.010	0–0.050	
12	0.195	0.082	0.034	0.014	0.051	$F=1$
12	0.168	0.059	0.021	0.008	0.051	$F=1$ ($\|x\|<0.057$ m) $F=0.3$ ($\|x\|\geqq 0.057$ m)
18	0.130	0.033	0.014	0.007	0.0095	

[a]Solution with $a=120.87$ Pa/K, $b=-3.2403$ Pa in Fig. 7 is same as that in Fig. 6 and also the same as solution with $q_{ht,m}=4000$ W/m^2 in Fig. 9.

The parameter r^i becomes zero when the truncated solution $T_w^{*(i)}$ approaches an exact solution. Table 2 shows $\bar{r}^i$, where $\bar{r}^i$ is the average value of r^i over the range of the horizontal axis of the corresponding figure for each order solution in Figs. 7, 9, 11, 12, and 18. The parameter $\bar{r}^i$ also becomes zero when the truncated solution $T_w^{*(i)}$ approaches an exact solution. From Table 2, $\bar{r}^i$ is found to be very small, at least for the third-order solution. As the order i increases, $\bar{r}^i$ decreases. The values of $\bar{r}^i$ in Table 2 suggest that the truncated solutions in the present study are convergent and effective. The parameters r^i or $\bar{r}^i$ would be useful for evaluating the convergence and the effectiveness of the solution.

Conclusions

A solution of the surface temperature and the runback water mass flow rate distributions for an electrothermal and a hot-air type anti-icing system of an aircraft is obtained by a modified perturbation method, where a small perturbation parameter α that represents the ratio of the external convective heat transfer rate from an airfoil surface to the internal heating rate is used. Because of the high nonlinearity in the energy equation, obtaining a convergent solution by a normal use of the perturbation method is virtually impossible. The calculation procedure is modified to improve the convergence properties of the solution. The main idea behind the modification is splitting of the nonlinear term into linear and nonlinear terms and introducing of a new variable ε by which α in each linear term is replaced. These modifications help reduce the contribution of the nonlinear term, which drastically improves the convergence characteristics of the solution.

The effectiveness of the analytical solution for an electrothermal and a hot-air anti-icing system is demonstrated. The solutions agreed well with the numerical results obtained by the Runge–Kutta method. The solutions also agreed relatively well with the numerical results by other anti-icing codes, CANICE and ANTICE, and agreed well with the icing test results on an airfoil model with an electrothermal anti-icing system.

At the least, the analytical solution in this paper would be effective if 1) α is small, 2) $P_{v,w}/P_e$ is small, 3) P_e does not change largely along the surface, and 4) $P_{v,w}$ is approximated properly by aT_w+b in a limited range of T_w. The convergence of the solution is examined by using the parameter $\bar{r}^i$. The solutions demonstrated in this paper are found to be convergent and effective.

The analytical solution obtained in this paper would be useful for the design of aircraft thermal anti-icing systems.

Acknowledgments

The author would like to thank Seiji Nishio and Eiji Shima of Kawasaki Heavy Industries, Ltd., and Shoji Umemoto of CRE Ltd. for their support of this paper. The author also would like to thank Masato Nagata of Kyoto University for his valuable advice for this paper.

References

[1]An SAE International Group, "Droplet Impingement and Ice Accretion Computer Codes," Society of Automotive Engineers, SAE Paper ARP5903, Oct. 2003.

[2]Ruff, G. A., and Berkowitz, B. M., "USERS Manual for the NASA Lewis Ice Accretion Prediction Code (LEWICE)," NASA CR-185129, May 1990.

[3]Beaugendre, H., Morency, F., and Habashi, W. G., "FENSAP-ICE's Three-Dimensional In-Flight Ice Accretion Module: ICE3D," *Journal of Aircraft*, Vol. 40, No. 2, 2003, pp. 239–247.

[4]Thomas, S. K., Cassoni, R. P., and MacArthur, C. D., "Aircraft Anti-Icing and De-Icing Techniques and Modeling," *Journal of Aircraft*, Vol. 33, No. 5, 1996, pp. 841–854.

[5]SAE Technical Committee, *SAE Aerospace Applied Thermodynamics Manual*, 2nd ed., Pts. 2C and 3F, ARP-1168, Society of Automotive Engineers, Inc., New York, 1969.

[6]Pfeifer, G. D., "Aircraft Engine Icing Technical Summary," *Icing Test for Aircraft Engines*, CP-236, AGARD, Rept. AD-A059452, Aug. 1978, pp. 9-1–9-17.

[7]Heinrich, A., Ross, R., and Ganesan, N., "Engine Inlet Anti-Icing System Evaluation Procedure," Federal Aviation Administration, FAA-RD-80-50, AD-A085179, Jan. 1980.

[8]Al-Khalil, K. M., Keith, T. G., Jr., De Witt, K. J., Nathman, J. K., and Dietrich, D. A., "Thermal Analysis of Engine Inlet Anti-Icing Systems," *Journal of Propulsion and Power*, Vol. 6, No. 5, 1990, pp. 628–634.

[9]Al-Khalil, K. M., "Numerical Simulation of an Aircraft Anti-Icing System Incorporating a Rivulet Model for the Runback Water," Ph.D. Dissertation, College of Engineering, Univ. of Toledo, Toledo, OH, June 1991.

[10]Al-Khalil, K. M., Keith, T. G., Jr., and De Witt, K. J., "New Concept in Runback Water Modeling for Anti-Iced Aircraft Surfaces," *Journal of Aircraft*, Vol. 30, No. 1, 1993, pp. 41–49.

[11]Al-Khalil, K. M., Keith, T. G., Jr., and De Witt, K. J., "Development of an Improved Model for Runback Water on Aircraft Surfaces," *Journal of Aircraft*, Vol. 31, No. 2, 1994, pp. 271–278.

[12]Morency, F., Tezok, F., and Paraschivoiu, I., "Anti-Icing System Simulation Using CANICE," *Journal of Aircraft*, Vol. 36, No. 6, 1999, pp. 999–1006.

[13]Morency, F., Tezok, F., and Paraschivoiu, I., "Heat and Mass Transfer in the Case of Anti-Icing System Simulation," *Journal of Aircraft*, Vol. 37, No. 2, 2000, pp. 245–252.

[14]Dillingh, J. E., and Hoeijmakers, H. W. M., "Numerical Simulation of Airfoil Ice Accretion and Thermal Anti-Icing Systems," 24th International Congress of the Aeronautical Sciences, Paper ICAS2004-7.5.2, Aug.–Sept. 2004.

[15]Nishio, S., and Kato, S., "Development of Ice Accretion and Anti-Icing System Simulation Code," 24th International Congress of the Aeronautical Sciences, Paper ICAS2004-7.5.R.2, Aug.–Sept. 2004.

[16]Gelder, T. F., and Lewis, J. P., "Comparison of Heat Transfer from Airfoil in Natural and Simulated Icing Conditions," NACA TN 2480, Sept. 1951.

[17]Al-Khalil, K. M., Horvath, C., Miller, D. R., and Wright, W. B., "Validation of NASA Thermal Ice Protection Computer Codes, Part 3—The Validation of ANTICE," AIAA Paper 97-0051, Jan. 1997.